Journal of Power Sources 196 (2011) 8850–8854

Contents lists available at ScienceDirect

Journal of Power Sources

journal homepage: www.elsevier.com/locate/jpowsour

Short communication

# Hybrid supercapacitor with nano-$TiP_2O_7$ as intercalation electrode

V. Aravindan[a,b], M.V. Reddy[b], S. Madhavi[a,c], S.G. Mhaisalkar[a,c], G.V. Subba Rao[b], B.V.R. Chowdari[b,*]

[a] Energy Research Institute, Nanyang Technological University, Research Techno Plaza, 50 Nanyang Drive, Singapore 637553, Singapore
[b] Department of Physics, National University of Singapore, Singapore 117542, Singapore
[c] School of Materials Science and Engineering, Nanyang Technological University, Singapore 639798, Singapore

ARTICLE INFO

*Article history:*
Received 1 April 2011
Received in revised form 15 May 2011
Accepted 27 May 2011
Available online 2 June 2011

*Keywords:*
Hybrid supercapacitor
Lithium ion battery
$TiP_2O_7$
Activated carbon

ABSTRACT

Nano-size (≤100 nm) $TiP_2O_7$ is prepared by the urea assisted combustion synthesis, at 450 and 900 °C. The compound is characterized by powder X-ray diffraction, Rietveld refinement, high resolution transmission electron microscopy and surface area methods. Lithium cycling properties by way of galvanostatic cycling and cyclic voltammetry (CV) showed a reversible and stable capacity of 60 (±3) mAh $g^{-1}$ (0.5 mole of Li) up to 100 cycles, when cycled at 15 mA $g^{-1}$ between 2–3.4 V vs. Li. Non-aqueous hybrid supercapacitor, $TiP_2O_7$ (as anode) and activated carbon (AC) (as cathode) has been studied by galvanostatic cycling and CV in the range, 0–3 V at 31 mA $g^{-1}$ and exhibited a specific discharge capacitance of 29 (±1) F $g^{-1}$ stable in the range, 100–500 cycles. The Ragone plot shows a deliverable maximum of 13 Wh $kg^{-1}$ and 371 W $kg^{-1}$ energy and power density, respectively.



## 1. Introduction

Of late, an increasing interest has been devoted to develop supercapacitors due to their high power application demands in many fields such as electric vehicles (EV), hybrid electric vehicles (HEV), off-peak energy back-up systems [1]. Based on their energy storage mechanism supercapacitors are classified into (i) electric double-layer capacitors (EDLCs) and (ii) pseudo-capacitors [2–4]. EDLC utilize an electrochemical double layer capacitance at the electrode/electrolyte interface (non-Faradaic process) where electric charges are accumulated on the electrode surface and ions of opposite charge are arranged in the electrolyte side. Carbon based materials are preferred as EDLC electrodes owing to their high surface area, relatively low cost, chemical stability in solutions of different pH and its amphoteric nature that allows rich electrochemical properties from donor to acceptor state, and wide range of operating temperatures [5,6]. Various forms of carbon have been studied as EDLC electrodes including allotropes (graphite, fullerenes/nanotubes), varied morphology (fibres, foams, fabrics) and microtextures [5,6]. In addition, transition metal oxides, like $MnO_2$ and $RuO_2$ or conducting polymers also have been employed as electrodes, which utilize the charge-transfer pseudo-capacitance. The EDLCs offer high power density, good reversibility and long cycle life in the aqueous medium. In contrast to EDLC, pseudocapacitors store charge Faradaically through transfer of charge between electrode (metal oxides/conducting polymers) and electrolyte accomplished through electrosorption, reduction–oxidation reactions, and intercalation processes. These Faradaic processes may allow pseudocapacitors to achieve greater capacitances, energy densities and good cycle life in comparison to EDLC. However, both EDLC and pseudocapacitors offer poor energy density (~10 Wh $kg^{-1}$) as compared to rechargeable batteries, like lithium ion batteries (100 Wh $kg^{-1}$).

Energy density of a supercapacitor is given by $E = CV^2/2$, where $C$ is the capacitance (F $g^{-1}$) and $V$ is the applied voltage. Based on this, there are two approaches to improve energy density of supercapacitors: (i) Use of non-aqueous electrolytes that offer higher operating voltages (~2–4 V) as compared to aqueous electrolytes (~1 V), and (ii) increase the capacitance ($C$) by incorporation of asymmetric electrode configuration, with battery-like electrode material (Faradaic process) along with EDLC electrode (non-Faradaic). This configuration is termed, "hybrid or asymmetric supercapacitor or hybrid electrochemical capacitor (HEC)" [1,3,6–9]. While the HEC employing aqueous electrolytes have been widely studied, there are also recent reports using non-aqueous solvents and Li-intercalating electrodes, like $Li[Ni_{0.5}Mn_{1.5}]O_4$ [10,11], $LiMn_2O_4$ [12], $LiFePO_4$ [13], $LiCoPO_4$ [14], $Li_2MnSiO_4$ [15], $Li_2FeSiO_4$ [16], $MnO_2$ [17], β-FeOOH [18], $Li_4Ti_5O_{12}$ [7,8,19,20], $TiO_2$-B [21] and $LiCrTiO_4$ [22]. Among them, $Li_4Ti_5O_{12}$ used as negative electrode (anode) is found to show very good HEC characteristics [8].

Titanium pyrophosphate, $TiP_2O_7$ has been studied as a Li-insertion host for the past few years which showed the reversible insertion and extraction of ~0.8 mole of Li per formula unit at a voltage of 2.6 V vs. Li [23–27]. To the best of our knowledge, $TiP_2O_7$ has not been studied in HEC configuration. In this paper, we have adopted a urea assisted combustion route to prepare $TiP_2O_7$

* Corresponding author. Tel.: +65 6516 2531; fax: +65 6777 6126.
*E-mail address:* phychowd@nus.edu.sg (B.V.R. Chowdari).

0378-7753/$ – see front matter © 2011 Elsevier B.V. All rights reserved.
doi:10.1016/j.jpowsour.2011.05.074

nanoparticles and have evaluated its Li-insertion properties vs. Li-metal and HEC configuration as anode with activated carbon (AC) as the counter electrode in non-aqueous electrolyte.

## 2. Experimental

For the synthesis of nano-$TiP_2O_7$, Ti metal powder (1.41 g, STREM, USA) was dissolved in $H_2O_2$ (30%, Merck, Germany) and ammonia solution (25% Merck, Germany) in a 2:1 volume ratio. After the complete dissolution of the Ti metal, $(NH_4)_2HPO_4$ (7.86 g, 99% Fisher) was added along with 6 moles of urea (99%, Aldrich) and the solution was slowly evaporated (~80 °C) on a hot plate to yield the precursor powder. The precursor was placed in the pre-heated box furnace (Carbolite, UK) at 450 °C for 30 min. A portion of it was subsequently calcined at 900 °C for 6 h in air. X-ray diffractometer (Philips X'Pert) equipped with Cu Kα radiation was used for structural characterization. The X-ray diffraction (XRD) data were refined by Rietveld refinement TOPAS-R (version 2.1) software. Morphological features were analyzed by transmission electron microscope (JEOL, JEM 3010). The Brunauer–Emmett–Teller (BET) surface area was measured using Micromeritics Tristar 3000, USA.

The composite electrode was prepared by mixing 70 wt.% of active material ($TiP_2O_7$), 15 wt.% of conducting additive (super P carbon) and 15 wt.% of binder (Kynar 2801) using *N*-methyl pyrrolidinone as solvent for the binder and the resulting slurry was coated on to Al foil (20 μm thickness) using doctor blade technique. The activated carbon (AC, BET surface area 880 (±20) $m^2\,g^{-1}$, Norit, Netherlands) electrode was prepared by a similar process with 80 wt.% AC, 10 wt.% super P carbon, and 10 wt.% binder on the Al foil substrate. The electrodes were dried, pressed between stainless steel twin rollers, and punched in to circular discs of 16 mm dia. The electrode discs were dried in a vacuum oven at 80 °C for 12 h to remove any residual solvent. The cells were assembled using 2016 coin cell configuration. Li-cycleability of $TiP_2O_7$ was tested against Li-metal (0.59 mm thick; Kyokuto Metal Co., Japan) which was separated by microporous glass fiber separator (Whatman, Cat. No. 1825 047, UK). Cyclic voltammetry (CV) was performed using metallic Li as reference and counter electrode at the slow scan rate of 58 $\mu V\,s^{-1}$ between 2 and 3.4 V using MacPile II (Biologic. France) system. The HEC was constructed using AC as positive electrode and $TiP_2O_7$ as negative electrode. The CVs were recorded for HEC between 0 and 3 V at various scan rates, 2–50 $mV\,s^{-1}$ using Solartron battery tester (Model no. 1470, UK). A solution of 1 M $LiPF_6$ in ethylene carbonate (EC) and dimethyl carbonate (DMC) (1:1 volume, Merck, Selectipur LP40) was used as the electrolyte. Galvanostatic profiles were recorded using Bitrode battery tester (SCN 12-4-5/18, USA).

## 3. Results and discussion

Combustion synthesis, also known as self-propagating high-temperature synthesis, is a convenient technique to produce nano-size oxides and has several advantages including simple, fast and energetically economic preparation, easy control of homogeneity and stoichiometry, ease of inclusion of substituent by virtue of the exothermic reaction and the associated gas evolution, and versatility in terms of the variety of fuels, like urea, ethylene glycol, hydrazine etc., that can be used for the synthesis [28]. The solution mixed starting materials decompose and react to form $TiP_2O_7$ evolving gases like $CO_2$, $N_2$ and $H_2O$, by virtue of the excess urea presently employed [29].

Powder X-ray diffraction (XRD) patterns of $TiP_2O_7$ prepared at 450 °C and at 900 °C are shown in Fig. 1 which indicate phase pure product. It is clear that the well-defined sharp and intense peaks are shown for $TiP_2O_7$ prepared at 900 °C. Both the patterns are indexed

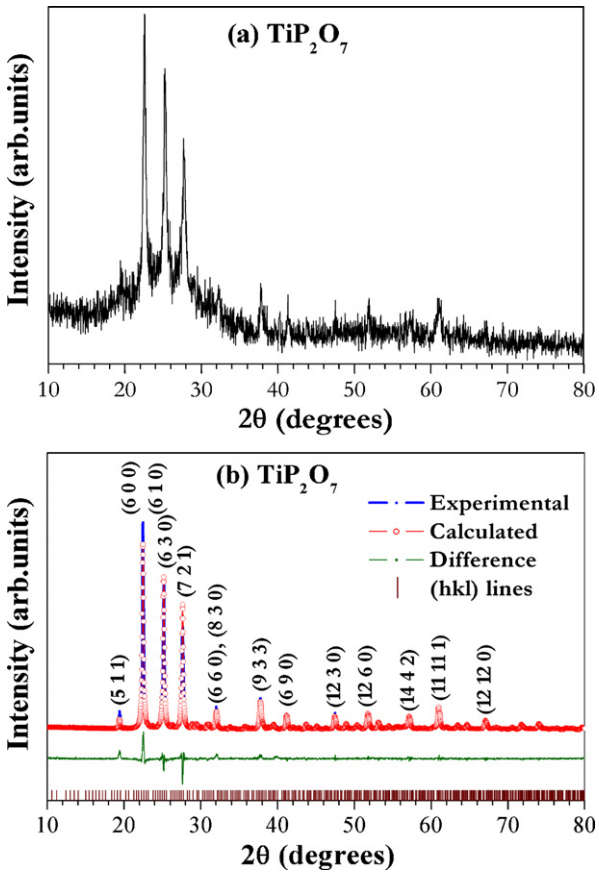


**Fig. 1.** X-ray diffraction pattern of nano-$TiP_2O_7$. (a) Prepared at 450 °C for 30 min in air (b) Prepared at 450 °C for 30 min and heat treated at 900 °C for 6 h in air. Miller indices and Rietveld-refinement-fitted pattern are shown.

according to the cubic $3 \times 3 \times 3$ super structure with $Pa\bar{3}$ space group. The XRD data of the 900 °C prepared compound is fitted by Rietveld refinement and the cubic lattice parameter, $a = 23.621$ (±0.0005) Å is in good agreement with that reported by Sanz et al. [30], Patoux and Masquelier [23] (23.632 Å) and the JCPDS data ($a = 23.6342$ Å; Card No. 38-1468). The Rietveld parameters are: $R_{wp} = 15.64$; $R_p = 12.18$; GOF = 1.37 and $R_{Bragg} = 4.94$. The crystallite size is calculated using Scherrer formula by the TOPAS software and found to be 56 (±1) nm. The site occupancies and thermal parameter values were fixed as per Sanz et al. [30] for the Rietveld refinement. The calculated pattern and the difference pattern are shown in Fig. 1b.

The TEM photograph of $TiP_2O_7$ (prepared at 900 °C) shows aggregated nano size (≤100 nm) particles (Fig. 2a). The HR-TEM lattice image, shown in Fig. 2b, indicates well-defined crystalline regions. The interplaner distance (*d*-spacing) is 0.349 (±0.01) nm, which agrees well with the *d*-value corresponding to the Miller indices (6 3 0) (Fig. 1). The BET surface area of $TiP_2O_7$ (prepared at 900 °C) is found to 12.6 (±0.2) $m^2\,g^{-1}$, which is typical of an oxide material heat treated at high temperature.

The cyclic voltammograms (CV) of nano-$TiP_2O_7$ (prepared at 900 °C) between 2 and 3.4 V vs. Li for the first five cycles are shown in Fig. 3. The initial scan was cathodic (Li-insertion) and the open circuit potential was ~3 V. As can be seen, Li insertion and extraction peaks are observed at 2.54 and 2.67 V, respectively. These values agrees well with 2.55 and 2.62 V, respectively reported by Patoux and Masquelier [23] from their galvanostatic cycling data. It is evident that the symmetrical form of CV traces indicates excellent reversibility of $TiP_2O_7$ for Li-insertion and extraction in good

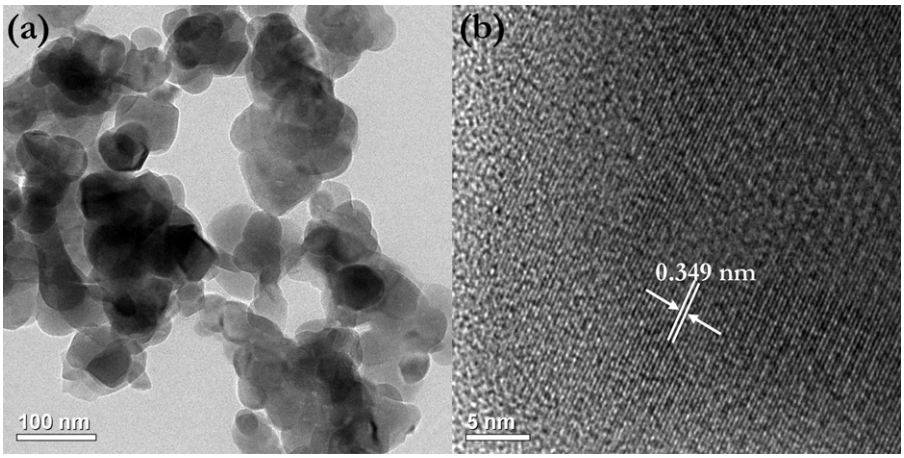


**Fig. 2.** TEM image of nano-$TiP_2O_7$ prepared at 900 °C and (b) the corresponding HR-TEM lattice image.

agreement with two-phase reaction mechanism, $TiP_2O_7 + xLi \leftrightarrow Li_x(Ti^{4+}_{1-x}Ti^{3+}_x)P_2O_7$ [23,26].

Galvanostatic cycling profiles of Li/$TiP_2O_7$ (prepared at 900 °C) cells were recorded at a constant current density of 15 mA $g^{-1}$ between 2 and 3.4 V at room temperature. Selected discharge–charge curves of 1, 5 and 50th cycles are shown in Fig. 4a. The distinct voltage plateaus at ~2.6 V are consistent with the CV measurements and are in agreement with two-phase reaction mechanism [23,26]. The measured first discharge capacity of 69 (±3) mAh $g^{-1}$ corresponds to the insertion of 0.58 mole of Li per formula unit against the theoretical capacity of 121 mAh $g^{-1}$ (1 mole of Li). The first-charge (Li-extraction) capacity is 60 (±3) mAh $g^{-1}$ and remains stable up to the 100th cycle, which corresponds to 0.5 mol of Li ($Li_{0.50}TiP_2O_7$) (Fig. 4b). The Li/$TiP_2O_7$ cell shows good current (*C*) rate capability: At 30 and 60 mA $g^{-1}$, a stable capacity of 48 (±3) and 37 (±3) mAh $g^{-1}$, respectively was observed (Fig. 4b).

The present results differ slightly from those reported in the literature. Uebou et al. [26] reported that $TiP_2O_7$ prepared at 700 °C by solid state reaction showed first discharge and charge capacities of ~95 and ~60 mAh $g^{-1}$, respectively. However, no cycling data were reported. Patoux and Masquelier [23] found that the $TiP_2O_7$ prepared by sol–gel technique showed a reversible capacity of ~100 mAh $g^{-1}$ (0.8 mole of Li) and stable up to 38 cycles when cycled between 2 and 3.4 V at C/10 rate. Shi et al. [24] reported that the mesoporous $TiP_2O_7$ obtained by sol–gel template route at temperatures 600, 700 and 800 °C exhibited initial reversible capacities ranging from 90 to 100 mAh $g^{-1}$ at 0.1 C current rate between 1.5 and 4 V, but capacity fading was observed in all cases, up to 10 cycles. A similar trend was observed at 1 C rate, from 10 to 20 cycles. Kishore et al. [25] prepared $TiP_2O_7$ by heating the precursor, $Ti(HPO_4)_2\ H_2O$ at 800 °C in air and reported that the compound showed a first-discharge capacity of 90 mAh $g^{-1}$ and

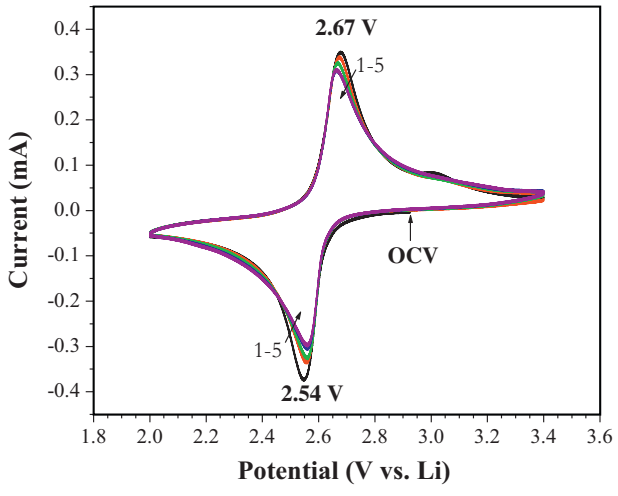


**Fig. 3.** Cyclic voltammograms of nano-$TiP_2O_7$, cycled between 2 and 3.4 V at the slow sweep rate of 58 μV $s^{-1}$. Metallic Li acts as both counter and reference electrode. The potentials are indicated. OCV refers to the open circuit voltage. Integer numbers indicate the cycle number.

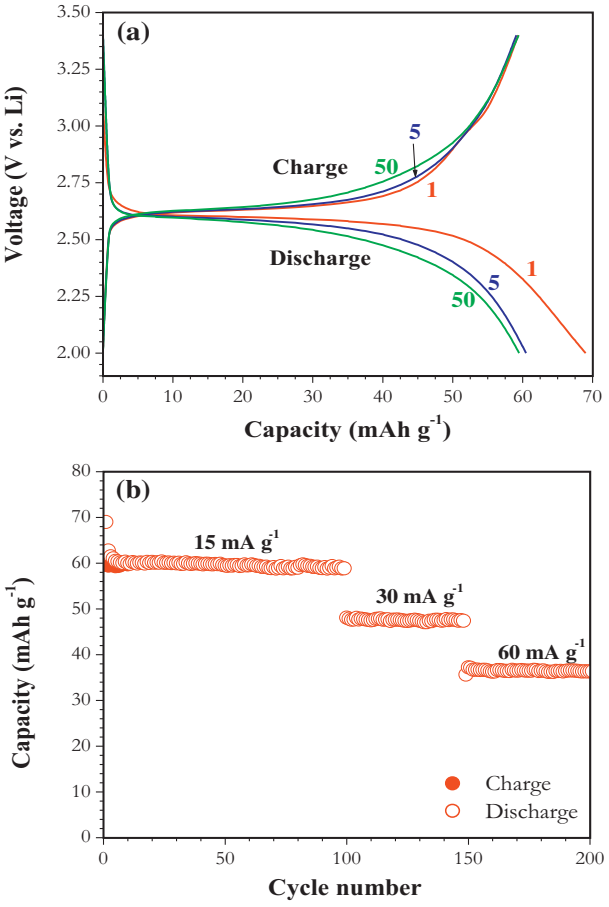


**Fig. 4.** (a) Galvanostatic discharge–charge profiles of nano-$TiP_2O_7$ between 2 and 3.4 V at 15 mA $g^{-1}$. Numbers indicate the cycle number. (b) Capacity vs. cycle number plot at various currents (15, 30 and 60 mA $g^{-1}$).

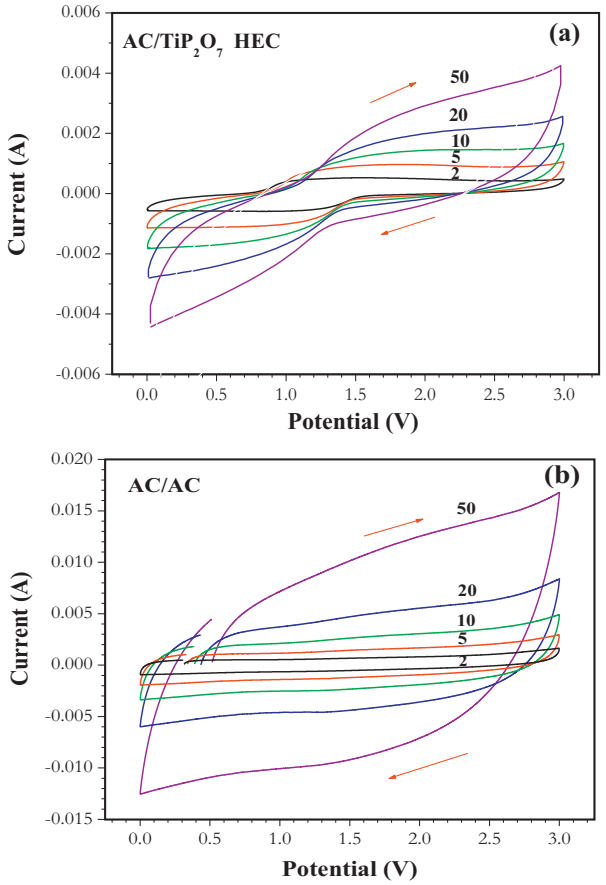


**Fig. 5.** (a) Cyclic voltammograms (CV) of the hybrid supercapacitor (HEC), AC (activated carbon)/$TiP_2O_7$, in which $TiP_2O_7$ is the negative electrode (intercalation electrode). (b) AC/AC symmetric supercapacitor. The CVs are recorded between 0 and 3 V in non-aqueous electrolyte. The numbers indicate the various sweep rates ($mV\,s^{-1}$).

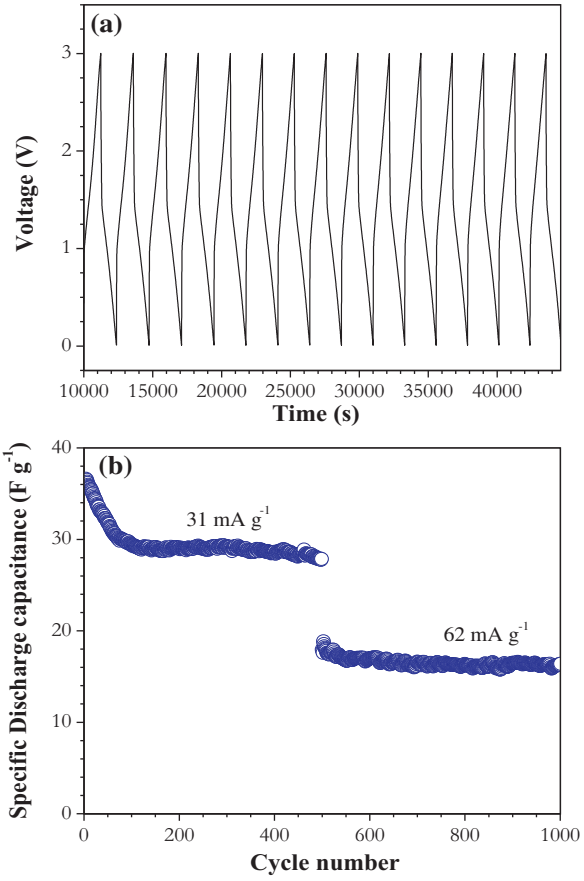


**Fig. 6.** Hybrid supercapacitor (HEC), AC/$TiP_2O_7$. (a) Galvanostatic charge–discharge curves at 31 mA $g^{-1}$ and (b) plot of the specific discharge capacitance ($C_{SP.HEC}$) vs. cycle number at currents, 31 and 62 mA $g^{-1}$.

a reversibly capacity of 63 mAh $g^{-1}$ which was stable between 5 and 25 cycles, when cycled at C/10 rate in the range, 1.5–3.5 V vs. Li. It may be mentioned that the galvanostatic performance of the 450 °C-synthesized $TiP_2O_7$ was not at all satisfactory and hence no further studies were carried out.

Fig. 5a shows the CVs of AC/$TiP_2O_7$ (prepared at 900 °C) HEC at various sweep rates from 2 to 50 mV $s^{-1}$ between 0 and 3 V, respectively. In order to compare the CV traces of AC/$TiP_2O_7$ HEC, AC/AC symmetric supercapacitor is constructed using the same electrolyte solution and studied in the same 0–3 V potential window, and their CV profiles are presented in Fig. 5b. The specific capacitance of the HEC ($C_{HEC}$) is calculated using the relation, $C_{HEC} = (\int i\Delta t = q)/V \cdot m$, where, $\Delta t$ is the time (s), $\Delta V$ is the potential difference ($V$), $m$ is the mass of the active materials used in both electrodes (13.04 mg for AC/$TiP_2O_7$), $q$ is the total charge (coulomb) obtained by integration of positive and negative sweep in the CV [31]. From the CV traces, the $C_{HEC}$ of 21, 15, 10, 7 and 4 F $g^{-1}$ were obtained for the sweep rates 2, 5, 10, 20 and 50 mV $s^{-1}$, respectively. Whereas, AC/AC system delivered the specific capacitance values of 31, 27, 24, 21 and 17 F $g^{-1}$ for 2, 5, 10, 20 and 50 mV $s^{-1}$ sweep rates, respectively (total mass of the electrode 18.4 mg). It was observed that the net charge ($q$) decreased with an increasing scan rate. Increasing the scan rate leads to Li-ion charge–discharge kinetics faster than the Li-ion diffusion in to the bulk resulting in decreased specific capacitance. It is pertinent to discuss the observed shapes of the CVs of the symmetric AC/AC and the HEC, AC/$TiP_2O_7$. The shape of the CVs of the AC/AC maintained almost the expected rectangular shapes at various sweep rates (Fig. 5b) [32]. However, the CV of AC/$TiP_2O_7$ exhibit a large deviation from the rectangular shape, especially at sweep rates larger than 5 mV $s^{-1}$ (Fig. 5a). This has been reproduced in duplicate measurements. This can be attributed to the fact that $TiP_2O_7$ as the anode in HEC, utilizes the Faradaic reaction of reversible Li-intercalation–de-intercalation and electron transfer, and more significantly, in a two-phase reaction, as is clear from Figs. 3 and 4. A similar deviation from the rectangular shapes of the CVs was observed by Wang et al. [21] in their study of the non-aqueous HEC, namely CNT (carbon nanotubes)/TNW ($TiO_2$ nano-wires), and it is known that TNW shows Li-storage and cyclability in a more or less single-phase reaction [33–35], which may also involve a pseudo-capacitive Li-storage [36]. Thus, we believe that the observed shapes of the CVs is mainly due to the Li-cyclability involving a two-phase Faradaic process in nano-$TiP_2O_7$.

The galvanostatic cycling performance of the AC/$TiP_2O_7$ (prepared at 900 °C) HEC between 0.0 and 3.0 V at a current of 31 mA $g^{-1}$ at room temperature is shown in Fig. 6a. The energy storage mechanism at the positive electrode (AC) utilizes non-Faradaic process (electrical double layer with the anion, $PF_6^-$ present in the electrolyte) and, as discussed above, a Faradaic reaction at the $TiP_2O_7$. Fig. 6b is the plot of specific discharge capacitance ($C_{SP.HEC}$) vs. cycle number of AC/$TiP_2O_7$ at currents of 31 and 62 mA $g^{-1}$ between 0 and 3.0 V. The discharge capacitance ($C_{cell}$) was calculated using the relations, $C_{cell} = (i \cdot t/\Delta V)$ and $C_{SP.HEC} = (4C_{cell}/m)$, where $i$ is the applied current (A), $t$ is discharge time (s) and $\Delta V$ is the potential difference (V) [14,37,38]. It can be seen that, the AC/$TiP_2O_7$ HEC delivers an initial discharge capacitance of 37 F $g^{-1}$ at 31 mA $g^{-1}$. This value decreases during the initial 100 cycles and thereafter, a stable $C_{SP.HEC}$ of 29 (±1) F $g^{-1}$ up to 500 cycles is seen. In the range,

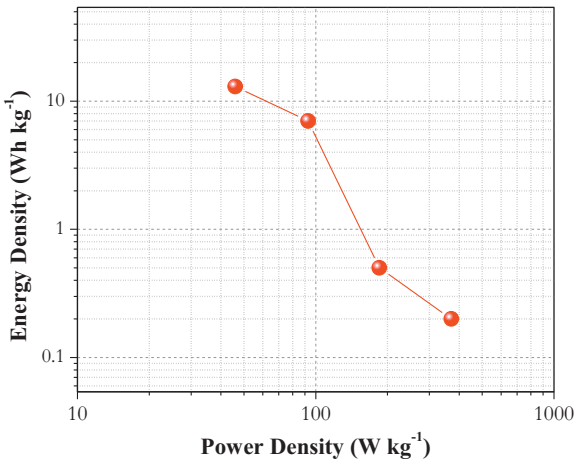


**Fig. 7.** Ragone plot of the HEC, AC/$TiP_2O_7$ from the data extracted from Fig. 6.

500–1000 cycles, a $C_{SP.HEC}$ of 17 (±1) F $g^{-1}$ at 62 mA $g^{-1}$ is observed with no noticeable capacity fade.

The specific energy density ($E_{SP}$) and specific power density ($P_{SP}$) of the AC/$TiP_2O_7$ HEC are calculated using the relations, $P_{SP} = (\Delta E \cdot i/m)$ and $E_{SP} = (P_{SP} \cdot t)$, where $\Delta E = (E_{max} + E_{min})/2$ and $E_{max}$ and $E_{min}$ are, respectively, the potential at the beginning of discharge and at the end of discharge [38]. The Ragone plot ($E_{SP}$ vs. $P_{SP}$) of the HEC is shown in Fig. 7 calculated from the data of Fig. 6. As can be seen, at an energy density of 13 Wh $kg^{-1}$ the corresponding power density is 46 W $kg^{-1}$. The Ragone plot also reveals an almost linear relationship. The observed values compare well with the electrochemical performance of the $Li_4Ti_5O_{12}$-based hybrid HEC in the non-aqueous electrolytes [7,9].

## 4. Conclusions

Urea assisted combustion synthesis route was employed for the preparation of nanosize (≤100 nm) $TiP_2O_7$. It is characterized by powder X-ray diffraction and Rietveld analysis, HR-TEM and surface area. Electrochemical Li-cycling showed that 0.5 mole of Li can be reversibly cycled with good current rate capability and stability up to 200 cycles. Cyclic voltammetry showed that the two-phase reaction occurs in $TiP_2O_7$ at 2.56 V (Li-insertion) and 2.67 V (Li-extraction) vs. Li. The hybrid supercapacitor, activated carbon (AC)/$TiP_2O_7$ in the non-aqueous electrolyte showed good cycling profiles and delivered maximum energy and power densities of 13 Wh $kg^{-1}$ and 371 W $kg^{-1}$, respectively at room temperature.

## Acknowledgements

This work is supported by the grants from Competitive Research Programme (CRP) of the National Research foundation (NRF, Singapore), number NRF-CRP4-2008-03 and the Ministry of Education (MOE), Singapore, grant number R-284-000-076-112.

## References

[1] C. Liu, F. Li, L.-P. Ma, H.-M. Cheng, Adv. Mater. 22 (2010) E28–E62.
[2] B.E. Conway, Electrochemical Supercapacitors: Scientific Fundamentals and Technological Applications, Springer, 1999.
[3] P. Simon, Y. Gogotsi, Nat. Mater. 7 (2008) 845–854.
[4] Y. Zhang, H. Feng, X. Wu, L. Wang, A. Zhang, T. Xia, H. Dong, X. Li, L. Zhang, Int. J. Hydrogen Energy 34 (2009) 4889–4899.
[5] M. Inagaki, H. Konno, O. Tanaike, J. Power Sources 195 (2010) 7880–7903.
[6] D.S. Su, R. Schlögl, ChemSusChem 3 (2010) 136–168.
[7] G.G. Amatucci, F. Badway, A. Du Pasquier, T. Zheng, J. Electrochem. Soc. 148 (2001) A930–A939.
[8] I. Plitz, A. Dupasquier, F. Badway, J. Gural, N. Pereira, A. Gmitter, G.G. Amatucci, Appl. Phys. A 82 (2006) 615–626.
[9] K. Naoi, P. Simon, Electrochem. Soc. Interface 17 (2008) 34–37.
[10] H. Li, L. Cheng, Y. Xia, Electrochem. Solid-State Lett. 8 (2005) A433–A436.
[11] H. Wu, C.V. Rao, B. Rambabu, Mater. Chem. Phys. 116 (2009) 532–535.
[12] S.B. Ma, K.W. Nam, W.S. Yoon, X.Q. Yang, K.Y. Ahn, K.H. Oh, K.B. Kim, Electrochem. Commun. 9 (2007) 2807–2811.
[13] X.L. Wu, L.Y. Jiang, F.F. Cao, Y.G. Guo, L.J. Wan, Adv. Mater. 21 (2009) 2710–2714.
[14] R. Vasanthi, D. Kalpana, N.G. Renganathan, J. Solid State Electrochem. 12 (2008) 961–969.
[15] K. Karthikeyan, V. Aravindan, S.B. Lee, I.C. Jang, H.H. Lim, G.J. Park, M. Yoshio, Y.S. Lee, J. Power Sources 195 (2010) 3761–3764.
[16] K. Karthikeyan, V. Aravindan, S.B. Lee, I.C. Jang, H.H. Lim, G.J. Park, M. Yoshio, Y.S. Lee, J. Alloys Compd. 504 (2010) 224–227.
[17] H.Q. Wang, Z.S. Li, Y.G. Huang, Q.Y. Li, X.Y. Wang, J. Mater. Chem. 20 (2010) 3883–3889.
[18] L. Cheng, H.Q. Li, Y.Y. Xia, J. Solid State Electrochem. 10 (2006) 405–410.
[19] K. Naoi, S. Ishimoto, Y. Isobe, S. Aoyagi, J. Power Sources 195 (2010) 6250–6254.
[20] L. Cheng, H.J. Liu, J.J. Zhang, H.M. Xiong, Y.Y. Xia, J. Electrochem. Soc. 153 (2006) A1472–A1477.
[21] Q. Wang, Z. Wen, J. Li, Adv. Funct. Mater. 16 (2006) 2141–2146.
[22] C.V. Rao, B. Rambabu, Solid State Ionics 181 (2010) 839–843.
[23] S. Patoux, C. Masquelier, Chem. Mater. 14 (2002) 5057–5068.
[24] Z. Shi, Q. Wang, W. Ye, Y. Li, Y. Yang, Micropor. Mesopor. Mater. 88 (2006) 232–237.
[25] M.S. Kishore, V. Pralong, V. Caignaert, U.V. Varadaraju, B. Raveau, J. Power Sources 169 (2007) 355–360.
[26] Y. Uebou, S. Okada, M. Egashira, J.I. Yamaki, Solid State Ionics 148 (2002) 323–328.
[27] H. Wang, K. Huang, Y. Zeng, S. Yang, L. Chen, Electrochim. Acta 52 (2007) 3280–3285.
[28] K.C. Patil, M.S. Hegde, T. Rattan, S.T. Aruna, Chemistry of Nanocrystalline Oxide Materials: Combustion Synthesis, Properties and Applications, World Scientific, Singapore, 2008.
[29] Y. Sharma, N. Sharma, G.V. Subba Rao, B.V.R. Chowdari, Electrochim. Acta 53 (2008) 2380–2385.
[30] J. Sanz, J.E. Iglesias, J. Soria, E.R. Losilla, M.A.G. Aranda, S. Bruque, Chem. Mater. 9 (1997) 996–1003.
[31] D. Xuan, W. Chengyang, C. Mingming, J. Yang, W. Jin, J. Phys. Chem. C 113 (2009) 2643–2646.
[32] P.C. Gao, A.-H. Lu, W.-C. Li, J. Power Sources 196 (2011) 4095–4101.
[33] A.R. Armstrong, G. Armstrong, J. Canales, P.G. Bruce, Angew. Chem. Int. Ed. 43 (2004) 2286–2288.
[34] A.R. Armstrong, G. Armstrong, J. Canales, P.G. Bruce, J. Power Sources 146 (2005) 501–506.
[35] T. Beuvier, M.R. Plouet, M.M.L. Granvalet, T. Brousse, O. Crosnier, L. Brohan, Inorg. Chem. 49 (2010) 8457–8464.
[36] M. Zukalová, M. Kalbáč, L. Kavan, I. Exnar, M. Graetzel, Chem. Mater. 17 (2005) 1248–1255.
[37] J.H. Park, O.O. Park, J. Power Sources 111 (2002) 185–190.
[38] J.Y. Luo, Y.Y. Xia, J. Power Sources 186 (2009) 224–227.